

## Article

# Structure and Properties of Porous $\text{Ti}_3\text{AlC}_2$ -Doped $\text{Al}_2\text{O}_3$ Composites Obtained by Slip Casting Method for Membrane Application

Egor Kashkarov <sup>1,\*</sup> , Maksim Krinitcyn <sup>1,2</sup> , Adilzhan Dyussambayev <sup>1</sup>, Alexey Pirozhkov <sup>1</sup> and Maksim Koptsev <sup>1</sup>

<sup>1</sup> School of Nuclear Science and Engineering, Tomsk Polytechnic University, 30 Lenina av., 634050 Tomsk, Russia

<sup>2</sup> Institute of Strength Physics and Materials Science SB RAS, 2/4, pr. Akademicheskii, 634055 Tomsk, Russia

\* Correspondence: ebk@tpu.ru; Tel.: +7-3822-70-17-77 (ext. 1562)

**Abstract:** In the present work, porous composites were fabricated from pure  $\text{Al}_2\text{O}_3$  and mixed  $\text{Ti}_3\text{AlC}_2/\text{Al}_2\text{O}_3$  powder by slip casting and sintering. The effect of sintering temperature and different composition ratio on microstructure, phase composition, porosity and gas permeation flux of the fabricated materials was investigated. The microstructure and phase composition of the samples were analyzed by scanning electron microscopy and X-ray diffraction, respectively. The gas permeation experiments were performed using pure hydrogen at 0.1–0.9 MPa pressure. It is shown that a decrease in sintering temperature from 1500 to 1350 °C results in an increase in hydrogen permeation flux of the alumina from 5 to 25 mol/( $\text{m}^2 \times \text{s}$ ), which is due to higher pore size and overall porosity of the samples. Sintering of  $\text{Ti}_3\text{AlC}_2/\text{Al}_2\text{O}_3$  powder mixtures leads to the formation of  $\text{Al}_2\text{O}_3$ ,  $\text{Al}_2\text{TiO}_5$  and  $\text{TiO}_2$  phases as a result of oxidation of the  $\text{Ti}_3\text{AlC}_2$  phase, resulting in an increased pore size in the composites compared with pure alumina. The open porosity of composites increases from 3.4 to 40% with an increasing  $\text{Ti}_3\text{AlC}_2/\text{Al}_2\text{O}_3$  ratio from 1/10 to 1/2, respectively. The composites with the highest porosity (40%) had a maximum permeation flux of 200 mol/( $\text{m}^2 \times \text{s}$ ). The changes in the bending strength of the alumina and composite samples, depending on the microstructure and porosity, were also discussed. The investigated composites are considered promising materials for hydrogen separation membrane supports.

**Keywords:** porous composites; alumina; mechanical properties; microstructure; ceramic supports



**Citation:** Kashkarov, E.; Krinitcyn, M.; Dyussambayev, A.; Pirozhkov, A.; Koptsev, M. Structure and Properties of Porous  $\text{Ti}_3\text{AlC}_2$ -Doped  $\text{Al}_2\text{O}_3$  Composites Obtained by Slip Casting Method for Membrane Application. *Materials* **2023**, *16*, 1537. <https://doi.org/10.3390/ma16041537>

Academic Editor: Oleg Shichalin

Received: 7 December 2022

Revised: 28 January 2023

Accepted: 6 February 2023

Published: 12 February 2023



**Copyright:** © 2023 by the authors. Licensee MDPI, Basel, Switzerland. This article is an open access article distributed under the terms and conditions of the Creative Commons Attribution (CC BY) license (<https://creativecommons.org/licenses/by/4.0/>).

## 1. Introduction

Currently, the issue of obtaining efficient and clean energy is very important. Hydrogen energy is one of the most promising areas for the development of alternative energy sources [1]. The commercial production of hydrogen usually results in low purity of hydrogen gas that cannot be used, for example, in fuel cells [2]. Therefore, different membrane systems are developed for hydrogen purification. The effective high-temperature membranes are made from palladium-based or other highly permeable metallic thin layers deposited on porous ceramic supports [3–5]. Ceramic supports should have high resistance to hydrogen embrittlement, suitable gas permeability and high mechanical strength [6].

Currently, one of the most effective supports is aluminum oxide due to low cost and chemical inertness to hydrogen and other gases [7,8]. The pores in aluminum oxide materials should be controlled to obtain good transportation properties for gas molecules diffused through the membranes [9]. MAX phases are a relatively new class of nanolaminated materials, generally described as  $\text{M}_{n+1}\text{AX}_n$  (where M—transition metal, A—element of A group (mostly IIIA and IVA), X—carbon and/or nitrogen,  $n = 1-3$ ). They are also promising as support material itself or in combination with other materials for supports and membranes due to their catalytic activity and combined properties of metals and ceramics, such as

high thermal and electrical conductivities, high mechanical properties, high-temperature oxidation and thermal shock resistance [10–14].  $\text{Ti}_3\text{AlC}_2$  MAX phase and  $\text{Al}_2\text{O}_3$  have the near-identical coefficients of thermal expansion, and  $\text{Ti}_3\text{AlC}_2/\text{Al}_2\text{O}_3$  composites have superior spallation resistance under service conditions [15]. This makes it possible to protect composites from cracking and destruction during repeated heating/cooling cycles. Since one of the mechanisms of oxidation of the MAX phase is the formation of a thin layer of  $\text{Al}_2\text{O}_3$ , the use of the MAX phase in a composite with  $\text{Al}_2\text{O}_3$  makes it possible to slow down the oxidation and form a strong bond between the particles of the MAX phase and  $\text{Al}_2\text{O}_3$  as a result of oxidation [16–19]. In addition, the introduction of MAX-phase particles into the  $\text{Al}_2\text{O}_3$  matrix increases the mechanical strength of the composites and the resistance to cracking [20,21]. The change in these and other properties directly depends on the microstructure and porosity of the material as well as its composition [22–24]. There are no experimental works on the microstructure, porosity and gas permeability of composites sintered from  $\text{Al}_2\text{O}_3$  and  $\text{Ti}_3\text{AlC}_2$  at different powder ratios. In this work, porous  $\text{Al}_2\text{O}_3$  and composite samples with different  $\text{Al}_2\text{O}_3$  and  $\text{Ti}_3\text{AlC}_2$  powder ratios are obtained by slip casting and sintering. The influence of the  $\text{Ti}_3\text{AlC}_2/\text{Al}_2\text{O}_3$  ratio on phase composition, microstructure, porosity and gas permeability of the obtained composites was investigated.

## 2. Experimental Details

### 2.1. Sample Preparation

The  $\text{Ti}_3\text{AlC}_2$  MAX-phase powder (98% purity,  $d_{50} = 5 \mu\text{m}$ ) was used in this work. As a source of  $\text{Al}_2\text{O}_3$ , waxed thermoplastic slip of corundum ceramics was used (VK-94.2 M7, the content of  $\text{Al}_2\text{O}_3$  was not less than 94 wt.%). This material can be used to obtain materials with different porosity depending on the sintering temperature, and it has a relatively low sintering temperature as well as stability of the thermomechanical properties in a wide temperature range.

The plasticized slurry contains paraffin in an amount of 12 wt.%, which had to be removed to obtain a dry powder. The removal of the paraffin binder was ensured by sintering the samples at a temperature of 800 °C. The removal took place in several successive stages. The first stage is drying at a temperature of 90 °C for 10 h. The second stage is a slow heating up to 300 °C for 12 h (17.5 K/h), followed by heating up to 800 °C for 4 h (125 K/h) with isothermal holding at 800 °C for 2 h.

The obtained samples were cleaned from filling and ground in a Pulverisette 6 Planetary Mono Mill (Fritsch, Idar-Oberstein, Germany) in a zirconia drum with zirconia grinding bodies until the material completely passed through a sieve with a mesh size of 0.063 mm.

$\text{Ti}_3\text{AlC}_2$  powder was mixed with  $\text{Al}_2\text{O}_3$  powder in mass ratios of 1/2, 1/4, 1/6, and 1/10, respectively. Mixing and homogenization of mixtures was carried out in a laboratory vibrating mill Pulverisette 23 (Fritsch, Germany) in a zirconia drum using zirconia grinding balls. The mass of the mixture for one mixing was 2 g, the oscillation frequency was 35 Hz, and the processing time was 5 min.

From the resulting mixtures, a composite was prepared with an alcohol solution of polyvinyl butyral binder (concentration—5%); the relative content of the binder in the press powder was 10 wt.%. Samples were made from composite on a laboratory press (LabTools, Saint-Petersburg, Russia) by uniaxial cold pressing (stainless steel die, diameter 12 mm); pressing pressure was 440 MPa. After that, the samples were dried to constant weight at a temperature of 70 °C.

The samples obtained were sintered at a temperature of 1350–1500 °C with a step of 50 °C in a shaft electric resistance furnace TK-27 1700Sh3F (Thermoceramics, Ekaterinburg, Russia) with lanthanum chromite heaters. The heating rate was 100 K/h, and the isothermal holding time was 2 h.

## 2.2. Characterization

The phase composition of the samples was analyzed by X-ray diffraction (XRD) using the XRD 7000S (Shimadzu, Tokyo, Japan) diffractometer equipped with a OneSight high-speed 1280-channel detector. The measurements were performed in Bragg–Brentano configuration using  $\text{CuK}\alpha$  radiation ( $\lambda = 0.154 \text{ nm}$ ) at 40 kV and 30 mA. A spectrum was acquired for each of the samples at the following parameters: scanning step—0.0143 deg; sample scanning speed—10 deg/min;  $2\theta$  angle range—10–70 deg. The microstructure and elemental composition of the samples were analyzed by scanning electron microscopy (SEM) using the Vega 3 (TESCAN, Brno, Czech Republic) equipped with an energy-dispersive X-ray spectroscopy (EDS) attachment.

The density of samples was determined using a hydrostatic weighing method (Archimedes method) in kerosene. The mechanical strength was measured by a three-point bending test performed using the Gotech AI-7000M machine (GoTech, Taichung City, Taiwan). For bending testing,  $2 \text{ mm} \times 2 \text{ mm} \times 18 \text{ mm}$  samples were cut from the specimens using a diamond disk. The Gotech data acquisition software was used to trigger the minimum load (0.1 N) on the sample and to start a data collection. The acquisition frequency was 124 Hz. The loading rate was set up as 0.5 mm/min according to the ASTM standard (E290). The span distance was equal to 16 mm.

## 2.3. Hydrogen Permeability Measurement

Hydrogen permeability tests were carried out using the Gas Reaction Automated Machine (GRAM, TPU, Tomsk, Russia) equipped with a gas permeation cell. For the hydrogen permeability test, the samples were placed in a test cell with a rubber sealing gasket. The active surface area of the specimens was  $1.9 \times 10^{-5} \text{ m}^2$ . The cell was evacuated to a residual pressure of  $1 \times 10^{-3} \text{ Pa}$  on both sides of the sample. The tests were performed at room temperature ( $25 \text{ }^\circ\text{C}$ ). On the gas supply side, the hydrogen pressure was set to 0.1–0.9 MPa. The gas pressure drop was measured on the precalibrated gas supply volume. The schematic diagram of the setup is shown in Figure 1.

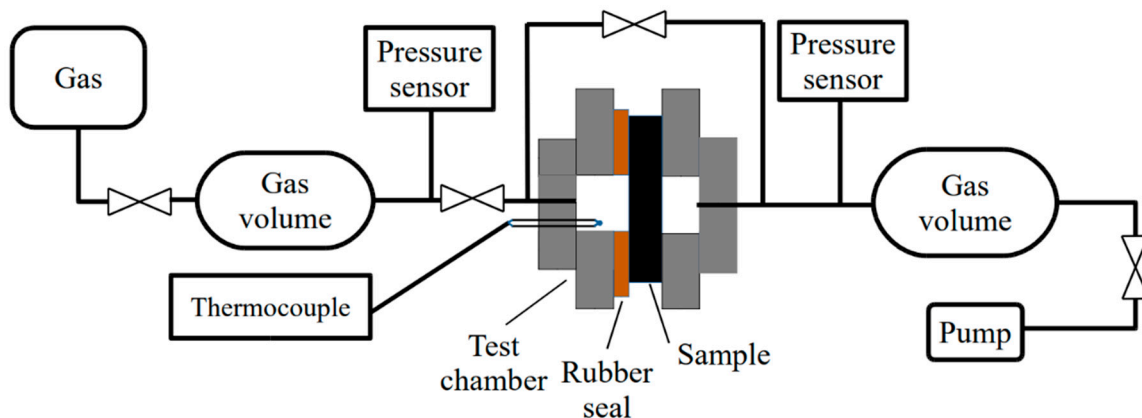


**Figure 1.** Schematic representation of the gas permeability cell.

The main characteristics of the supports and membranes are gas flow and permeability. Flux ( $\Phi$ ) is the total transport of a substance across a membrane and can be expressed as mass or molar concentration per unit time per unit area. Permeability ( $J$ ) is defined as flow per unit pressure difference between the inlet and outlet side of the membrane. This is shown in the following equation:

$$j = \Phi \times \frac{d}{\Delta P},$$

where  $\Phi$ —gas flow ( $\text{mol}/(\text{m}^2 \times \text{s})$ ),  $J$ —gas permeability ( $\text{mol}/(\text{m} \times \text{s} \times \text{Pa})$ ),  $d$ —sample thickness (m),  $\Delta P$ —pressure difference at the inlet and outlet of the sample (Pa).

### 3. Results and Discussion

#### 3.1. Microstructure and Phase Composition

The XRD patterns for the green bodies and sintered samples are shown in Figure 2. For sintered aluminum oxide samples, only the  $\alpha$ - $\text{Al}_2\text{O}_3$  phase was found at all the sintering temperatures (Figure 2a). The as-received green bodies of composite samples are represented by the  $\alpha$ - $\text{Al}_2\text{O}_3$  and hexagonal closed-packed  $\text{Ti}_3\text{AlC}_2$  phases (Figure 2b). The increase in intensities of the corresponding peaks of the  $\text{Ti}_3\text{AlC}_2$  phase indicates its higher volume content at a higher  $\text{Ti}_3\text{AlC}_2/\text{Al}_2\text{O}_3$  powder ratio. After sintering, the  $\text{Ti}_3\text{AlC}_2$  phase undergoes oxidation during sintering of  $\text{Ti}_3\text{AlC}_2/\text{Al}_2\text{O}_3$  composites (Figure 2c), which resulted in the formation of  $\text{Al}_2\text{TiO}_5$  and  $\text{TiO}_2$  oxide phases [13–16]. The results of phase composition analysis are presented in Table 1. Since no secondary phases were observed for pure aluminium and the lattice parameters did not change after the sintering, the data for these samples are not included in Table 1. It can be seen that the content of the oxide  $\text{Al}_2\text{TiO}_5$  and  $\text{TiO}_2$  phases in the sintered composite samples increases with increasing  $\text{Ti}_3\text{AlC}_2/\text{Al}_2\text{O}_3$  powder ratio.

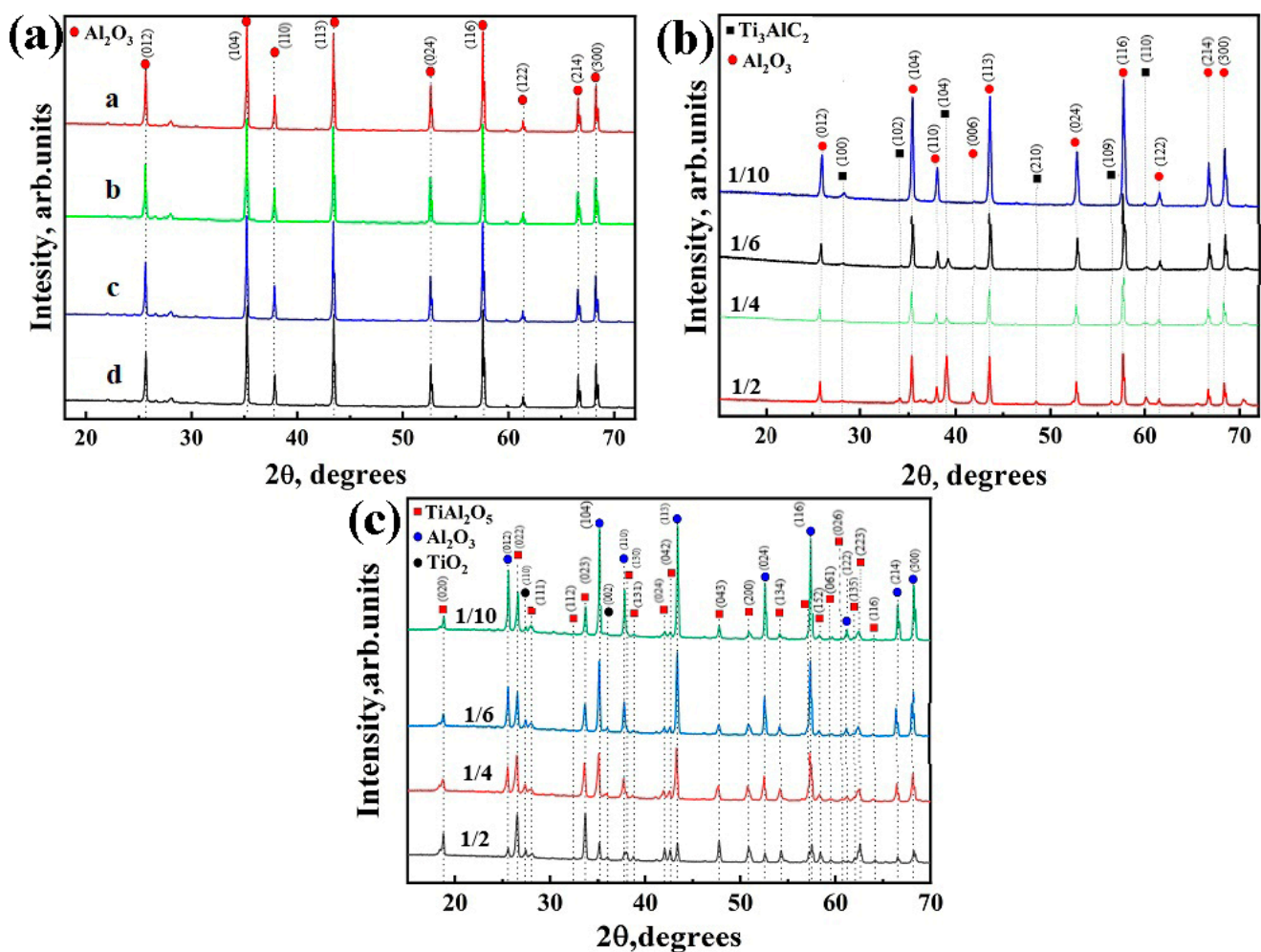


**Figure 2.** XRD patterns of (a) porous  $\text{Al}_2\text{O}_3$  at different sintering temperatures: a—1500 °C, b—1450 °C, c—1400 °C, d—1350 °C; (b) green bodies before sintering and (c) porous composites obtained from  $\text{Ti}_3\text{AlC}_2/\text{Al}_2\text{O}_3$  powders.

**Table 1.** Phase composition of the composite samples calculated from XRD data.

Sample Name	Phase	Content, %	Lattice Parameters, Å	Phase	Content, %	Lattice Parameters, Å
Composite 1/2	Al <sub>2</sub> O <sub>3</sub>	62	a = 4.763 c = 13.005	Al <sub>2</sub> O <sub>3</sub>	16	a = 4.752 c = 12.979
	Ti <sub>3</sub> AlC <sub>2</sub>	38	a = 3.087 c = 18.588	TiO <sub>2</sub>	5	a = 4.588 c = 2.966
Composite 1/4	Al <sub>2</sub> O <sub>3</sub>	81	a = 4.761 c = 12.998	TiAl <sub>2</sub> O <sub>5</sub>	79	a = 3.586 b = 9.430 c = 9.641
	Ti <sub>3</sub> AlC <sub>2</sub>	19	a = 3.075 c = 18.560	Al <sub>2</sub> O <sub>3</sub>	34	a = 4.761 c = 12.999
Composite 1/6	Al <sub>2</sub> O <sub>3</sub>	88	a = 4.762 c = 13.001	TiO <sub>2</sub>	6	a = 4.598 c = 2.966
	Ti <sub>3</sub> AlC <sub>2</sub>	12	a = 3.080 c = 18.569	TiAl <sub>2</sub> O <sub>5</sub>	60	a = 3.590 b = 9.449 c = 9.659
Composite 1/10	Al <sub>2</sub> O <sub>3</sub>	93	a = 4.762 c = 12.999	Al <sub>2</sub> O <sub>3</sub>	45	a = 4.760 c = 12.997
	Ti <sub>3</sub> AlC <sub>2</sub>	7	a = 3.077 c = 18.565	TiO <sub>2</sub>	7	a = 4.597 c = 2.962
Composite 1/10	Al <sub>2</sub> O <sub>3</sub>	93	a = 4.762 c = 12.999	TiAl <sub>2</sub> O <sub>5</sub>	48	a = 3.590 b = 9.449 c = 9.662
	Ti <sub>3</sub> AlC <sub>2</sub>	7	a = 3.077 c = 18.565	Al <sub>2</sub> O <sub>3</sub>	49	a = 4.761 c = 12.996
Composite 1/10	Al <sub>2</sub> O <sub>3</sub>	93	a = 4.762 c = 12.999	TiO <sub>2</sub>	4	a = 4.582 c = 2.959
	Ti <sub>3</sub> AlC <sub>2</sub>	7	a = 3.077 c = 18.565	TiAl <sub>2</sub> O <sub>5</sub>	47	a = 3.591 b = 9.451 c = 9.659

The microstructural analysis of the sintered Al<sub>2</sub>O<sub>3</sub> porous ceramics showed that pore size and overall porosity decrease with increasing sintering temperature. The measured open porosity by the Archimedes method decreased from 37 to 21% when the sintering temperature increased from 1350 to 1500 °C, respectively (Table 2). At the same time, the apparent density of Al<sub>2</sub>O<sub>3</sub> samples increased from 2.31 to 3.07 g/cm<sup>3</sup>, while the average pore size decreased from 1.25 to 0.5 μm.

The addition of the MAX phase leads to the formation of more open pores in the composites (Figure 3). The average pore size increased from ~0.5 to 6.5 μm with increasing powders ratio from 1/10 to 1/2. It should be noted that the pores have rounded and elongated shapes. The presence of the MAX phase changes the sintering kinetics as well as the microstructure of the composite samples (Figure 4). In addition to the sintering process, the decomposition and oxidation of the MAX phase proceed at high temperatures. The formation of the Al<sub>2</sub>TiO<sub>5</sub> phase from titanium and aluminum in oxygen ( $\Delta G = -2640.1 + 0.5T$  kJ/mol) is more likely than the formation of Al<sub>2</sub>O<sub>3</sub> ( $\Delta G = -1692.5 + 0.33T$  kJ/mol) and TiO<sub>2</sub> ( $\Delta G = -940.4 + 0.181T$  kJ/mol) [25]. Thus, during the sintering processes, energy is spent on the decomposition of the MAX phase, as well as on other processes, which deintensifies the sintering kinetics. The formation of new phases during sintering of a mixture of powders with different thermal expansion coefficients will also prevent the formation of strong bonds between the particles. In addition, the formed particles are different in size, shape

and chemical nature, which also affects the sintering kinetics and the final microstructure and porosity of the composites.

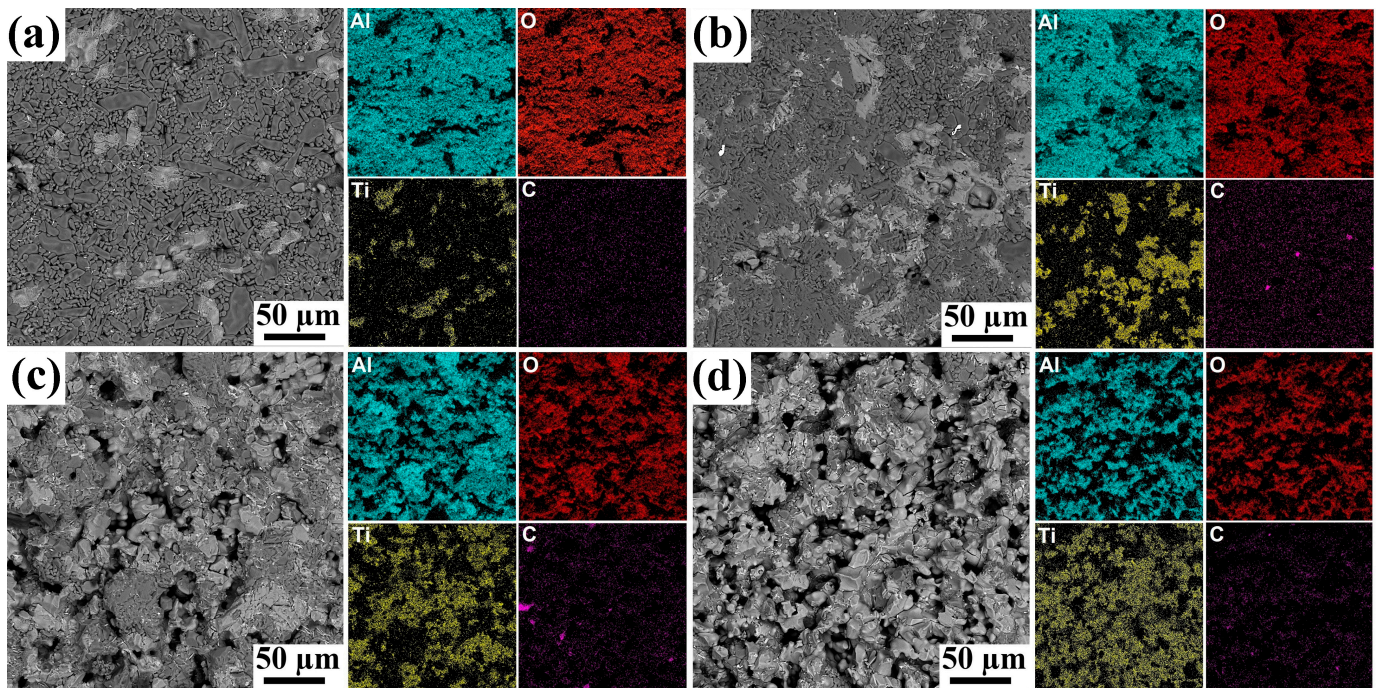


**Figure 3.** SEM images and corresponding EDS elemental maps for porous composites obtained from  $\text{Ti}_3\text{AlC}_2/\text{Al}_2\text{O}_3$  mixture: 1/10 (a), 1/6 (b), 1/4 (c) and 1/2 (d).

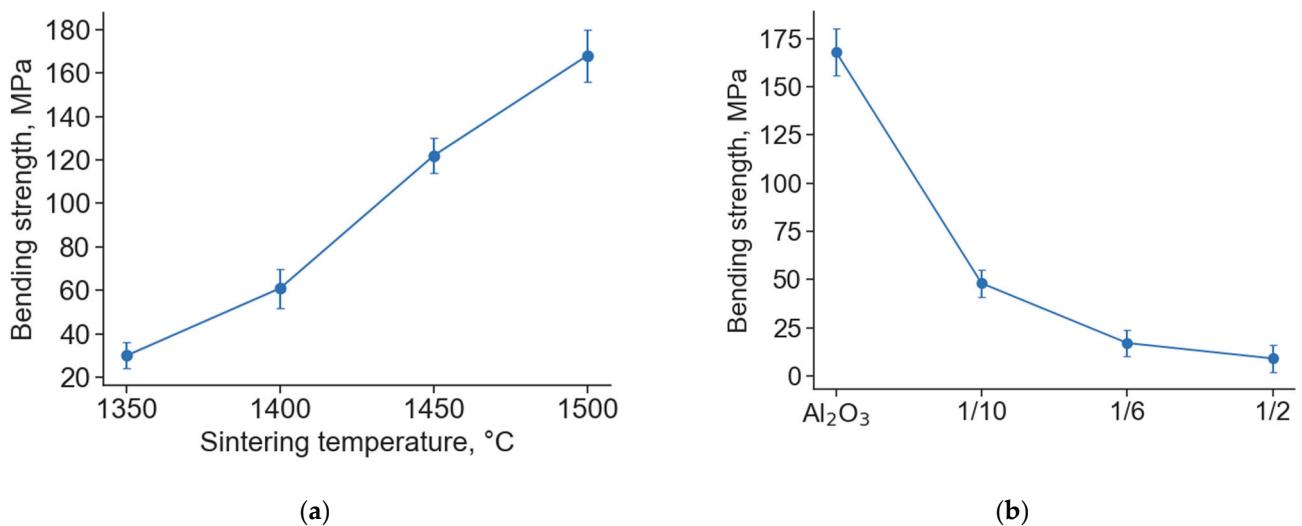


**Figure 4.** Bending strength of  $\text{Al}_2\text{O}_3$  samples after sintering in air at different temperatures (a) and bending strength of samples of pure  $\text{Al}_2\text{O}_3$  and mixtures of  $\text{Ti}_3\text{AlC}_2/\text{Al}_2\text{O}_3$  after sintering in air at 1500 °C (b).

The microstructure of the composites is represented by the alumina phase (dark contrast) and  $\text{TiO}_2 + \text{Al}_2\text{TiO}_5$  phase (bright contrast) (Figure 3). EDS analysis revealed that the increase in  $\text{Ti}_3\text{AlC}_2$  content results in a more homogeneous distribution of the oxide phases and a more uniform distribution of pores in the composites. The content of the oxide phases formed from MAX-phase oxidation increases with the  $\text{Ti}_3\text{AlC}_2/\text{Al}_2\text{O}_3$  ratio that is well correlated with XRD data. The distribution of these oxides is more uniform at higher ratios of  $\text{Ti}_3\text{AlC}_2$  to alumina powders. The open porosity increases from 3.4 to

40% with an increase in the powder ratio from 1/10 to 1/2, respectively (Table 2). At the given sintering temperature, a more uniform porous structure was formed only at 1/4 and 1/2 powder ratios.

**Table 2.** The apparent density, open porosity and water absorption of the samples measured by the Archimedes method.

Sample	Water Absorption, %	Porosity, %	Open Porosity, %	Apparent Density, g/cm <sup>3</sup>	Average Pore Size, μm
Composite 1/2	15.7	-	40.1	2.01	6.5
Composite 1/4	7.8	-	27.2	2.76	4
Composite 1/6	3.4	-	14.0	3.27	3.5
Composite 1/10	0.8	-	3.4	3.54	<0.5
Al <sub>2</sub> O <sub>3</sub> 1350 °C	12.7	41.3	37.1	2.32	1.25
Al <sub>2</sub> O <sub>3</sub> 1400 °C	10.8	37.7	33.5	2.46	0.85
Al <sub>2</sub> O <sub>3</sub> 1450 °C	8.2	31.1	28.3	2.72	0.65
Al <sub>2</sub> O <sub>3</sub> 1500 °C	5.5	22.3	21.4	3.07	0.5

The results showed that variation of the Ti<sub>3</sub>AlC<sub>2</sub>/Al<sub>2</sub>O<sub>3</sub> ratio makes it possible to control the porosity of the resulting samples, ranging from relatively dense to highly porous composites.

### 3.2. Mechanical Properties

Figure 4 shows the results of bending strength measurements for both pure Al<sub>2</sub>O<sub>3</sub> (sintered at different temperatures) and composite samples obtained from Ti<sub>3</sub>AlC<sub>2</sub>/Al<sub>2</sub>O<sub>3</sub> mixtures.

For pure Al<sub>2</sub>O<sub>3</sub> samples, the bending strength increases from 25 to 165 MPa with an increasing sintering temperature from 1350 to 1500 °C, respectively (Figure 4). We used a commercial Al<sub>2</sub>O<sub>3</sub> powder for which the manufacturer recommended a sintering temperature of 1580 ± 30 °C to obtain dense material. Lower sintering temperatures were used to obtain a microporous structure of the material and to analyze the influence of its porosity on the bending strength. It was demonstrated that the strength of all investigated Al<sub>2</sub>O<sub>3</sub> samples remains at a sufficiently high level compared with alumina support materials with similar density produced in other works [26–28]. The bending strengths of the alumina samples with acceptable porosity for support material (obtained at 1350 and 1400 °C) were 25 and 60 MPa, respectively.

The bending strength of the composite samples decreased from 50 to 10 MPa with increasing Ti<sub>3</sub>AlC<sub>2</sub>/Al<sub>2</sub>O<sub>3</sub> powder ratios from 1/10 to 1/2, respectively (Figure 4b). The analysis of microstructure and porosity showed that the porosity of the composites increased with the Ti<sub>3</sub>AlC<sub>2</sub>/Al<sub>2</sub>O<sub>3</sub> powder ratio. Thus, it is assumed that the main reason for the reduction in strength is the change in porosity of the composite samples. In addition, at comparable porosity values, the strength of the composites is lower than that of pure alumina samples. This indirectly confirms the weaker bonding between the particles and the possible internal stresses in the composite samples.

### 3.3. Hydrogen Permeability

The permeability tests show the dependence between hydrogen permeation flux through the samples and gas pressure (Figure 5). The results showed near linear dependence of hydrogen flux on pressure for all the alumina samples (Figure 5a). The flow rate increases from 5 to 25 mol/(m<sup>2</sup> × s) (0.9 MPa pressure) when the sintering temperature increases from 1350 to 1500 °C, respectively. Thus, the increase in porosity of Al<sub>2</sub>O<sub>3</sub> results in a fivefold higher gas flow through the samples (Figure 5a). It can be seen that the increase in the Ti<sub>3</sub>AlC<sub>2</sub>/Al<sub>2</sub>O<sub>3</sub> ratio and the corresponding porosity result in higher hydrogen flux through the samples. Similar dependence between the flux and gas pressure was found for all the samples in the investigated hydrogen pressure range. The hydrogen flux for the sample with 1/10 ratio is in the range of 0.06–0.4 mol/(m<sup>2</sup> × s), which is relatively low for support materials. The maximum flow of 30–200 mol/(m<sup>2</sup> × s) was achieved for the

sample with the highest porosity (1/2 ratio), which is suitable for ceramic-based supports developed for gas separation membranes [29].

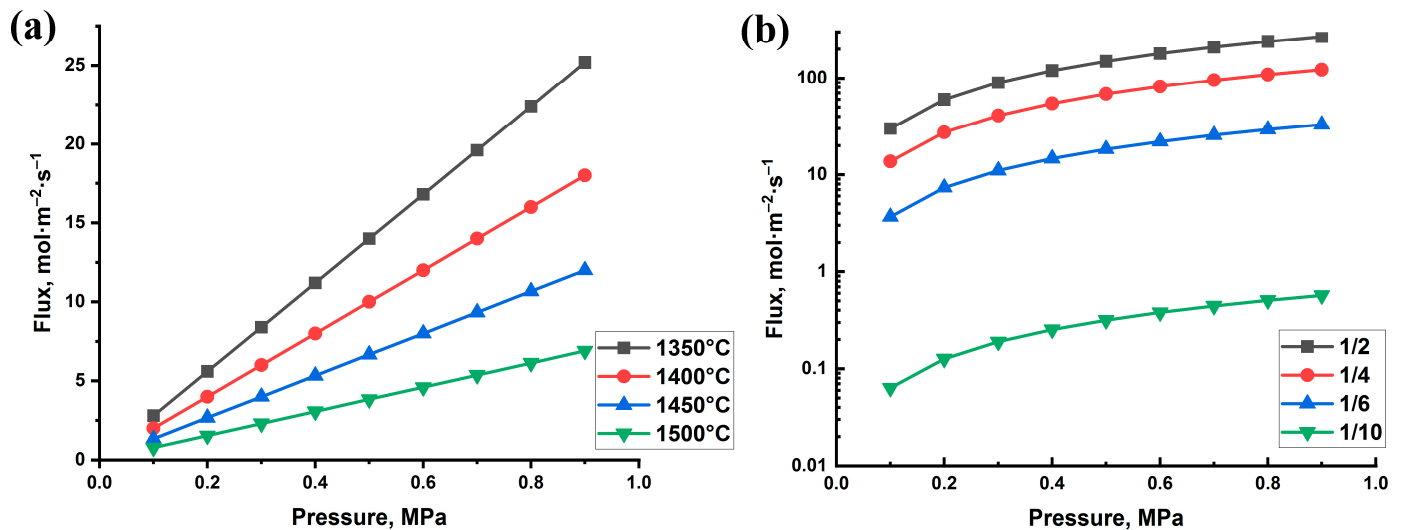


**Figure 5.** Hydrogen permeation flux depending on pressure for the porous samples obtained from pure Al<sub>2</sub>O<sub>3</sub> (a) and Ti<sub>3</sub>AlC<sub>2</sub>/Al<sub>2</sub>O<sub>3</sub> powder mixtures (b).

The flux of hydrogen through a thin film of palladium (0.117–50 μm) at a temperature of 500 °C with a pressure difference of 0.2 MPa and a permeability of  $1.9 \times 10^{-8}$  (mol/(m × s × Pa)) will be 0.17–72 mol/(m<sup>2</sup> × s) [30,31]. When the hydrogen flux through the ceramic substrate is 1–80 mol/(m<sup>2</sup> × s) at a thickness of 3 mm, the hydrogen flux will be limited only by a dense layer of palladium. In [32], the hydrogen flux through the 1 mm thick porous Al<sub>2</sub>O<sub>3</sub> substrate embedded in a porous stainless steel base was 0.002 mol/(m<sup>2</sup> × s). Checchetto et al. [33] used Al<sub>2</sub>O<sub>3</sub> with a thickness of 60 μm; the hydrogen flux was 0.15 mol/(m<sup>2</sup> × s) at a pressure difference of 0.1 MPa. Thus, the fabricated alumina and composite samples have high hydrogen permeability at a thickness of 2–3 mm and good mechanical strength.

#### 4. Conclusions

Porous composites were fabricated from pure alumina and mixed Ti<sub>3</sub>AlC<sub>2</sub> and Al<sub>2</sub>O<sub>3</sub> powders by slip casting. The influence of alumina sintering temperature and Ti<sub>3</sub>AlC<sub>2</sub>/Al<sub>2</sub>O<sub>3</sub> powder ratio on microstructure, porosity and gas permeability of the fabricated porous materials was analyzed. The following conclusions were made:

1. The decrease in sintering temperature from 1500 to 1350 °C results in an increase in the porosity of alumina samples from 21 to 37% and an increase in their pore size. The hydrogen permeation flux increases up to 25 mol/(m<sup>2</sup> × s) for alumina samples sintered at 1350 °C.
2. The addition of Ti<sub>3</sub>AlC<sub>2</sub> to alumina powder leads to the formation of composite oxide ceramics with higher pore size. The phase composition of the sintered composites is represented by Al<sub>2</sub>O<sub>3</sub>, TiO<sub>2</sub> and Al<sub>2</sub>TiO<sub>5</sub> phases and is caused by oxidation of the Ti<sub>3</sub>AlC<sub>2</sub> phase. The distribution of the oxides formed from the Ti<sub>3</sub>AlC<sub>2</sub> phase is more uniform at higher ratios of MAX phase to alumina powders.
3. The porosity of composites increases from 3.4 to 40% with increasing the Ti<sub>3</sub>AlC<sub>2</sub>/Al<sub>2</sub>O<sub>3</sub> powder ratio from 1/10 to 1/2, respectively. The increase in porosity of composites provides better gas permeability. The maximum hydrogen flux up to 200 mol/(m<sup>2</sup> × s) was achieved for the sample with the highest porosity of 40%.
4. The bending strength of the sintered samples decreases with the addition of MAX phase to alumina powder but increases the gas permeability. All the fabricated



materials demonstrate relatively high bending strength, which was 25 and 10 MPa for highly porous alumina (37%) and composite (40%) materials. The fabricated materials can be used for membrane support application.

**Author Contributions:** Conceptualization, M.K. (Maksim Krinitcyn), E.K. and A.D.; funding acquisition, E.K.; formal analysis, A.P., M.K. (Maksim Krinitcyn) and M.K. (Maksim Koptsev); investigation, E.K.; methodology, M.K. (Maksim Krinitcyn), A.D. and M.K. (Maksim Koptsev); visualization, A.P., M.K. (Maksim Koptsev); supervision, E.K.; writing—original draft, A.D. and A.P.; writing—review and editing, E.K. and M.K. (Maksim Krinitcyn); project administration, E.K., M.K. (Maksim Krinitcyn). All authors have read and agreed to the published version of the manuscript.

**Funding:** The research was supported by the Governmental Program, project No. FSWW-2021-0017.

**Institutional Review Board Statement:** Not applicable.

**Informed Consent Statement:** Not applicable.

**Data Availability Statement:** Data are contained within the article.

**Acknowledgments:** The authors thank Sharif Sharafeev for porosity measurements.

**Conflicts of Interest:** The authors declare no conflict of interest.

## References

1. Sharma, S.; Ghoshal, S.K. Hydrogen the future transportation fuel: From production to applications. *Renew. Sustain. Energy Rev.* **2015**, *43*, 1151–1158. [[CrossRef](#)]
2. Li, P.; Chen, H.Z.; Chung, T.S. The effects of substrate characteristics and pre-wetting agents on PAN–PDMS composite hollow fiber membranes for CO<sub>2</sub>/N<sub>2</sub> and O<sub>2</sub>/N<sub>2</sub> separation. *J. Membr. Sci.* **2013**, *434*, 18–25. [[CrossRef](#)]
3. Liang, C.Z.; Chung, T.S.; Lai, J.Y. A review of polymeric composite membranes for gas separation and energy production. *Prog. Polym. Sci.* **2019**, *97*, 101141. [[CrossRef](#)]
4. Kashkarov, E.; Krotkevich, D.; Koptsev, M.; Ognev, S.; Svyatkin, L.; Travitzky, N.; Lider, A. Microstructure and Hydrogen Permeability of Nb-Ni-Ti-Zr-Co High Entropy Alloys. *Membranes* **2022**, *12*, 1157. [[CrossRef](#)]
5. Jokar, S.M.; Farokhnia, A.; Tavakolian, M.; Pejman, M.; Parvasi, P.; Javanmardi, J.; Basile, A. The recent areas of applicability of palladium-based membrane technologies for hydrogen production from methane and natural gas: A review. *Int. J. Hydrogen Energy* **2023**, *48*, 6451–6476. [[CrossRef](#)]
6. Abate, S.; Genovese, C.; Perathoner, S.; Centi, G. Performances and stability of a Pd-based supported thin film membrane prepared by EPD with a novel seeding procedure. Part 1—Behaviour in H<sub>2</sub>:N<sub>2</sub> mixtures. *Catal. Today* **2009**, *145*, 63–71. [[CrossRef](#)]
7. Tanaka, D.P.; Medrano, J.A.; Sole, J.V.; Gallucci, F. *Metallic Membranes for Hydrogen Separation. Current Trends and Future Developments on (Bio-) Membranes*; Elsevier: Amsterdam, The Netherlands, 2020; pp. 1–29.
8. Tosti, S. Supported and laminated Pd-based metallic membranes. *Int. J. Hydrogen Energy* **2003**, *28*, 1445–1454. [[CrossRef](#)]
9. Wałowski, G. Assessment of gas permeability coefficient of porous materials. *J. Sustain. Min.* **2017**, *16*, 55–65. [[CrossRef](#)]
10. Sun, Z.M. Progress in research and development on MAX phases: A family of layered ternary compounds. *Int. Mater. Rev.* **2011**, *56*, 143–166. [[CrossRef](#)]
11. Barsoum, M.W.; Radovic, M. Elastic and mechanical properties of the MAX phases. *Ann. Rev. Mater. Res.* **2011**, *41*, 195–227. [[CrossRef](#)]
12. Lyu, J.; Kashkarov, E.B.; Travitzky, N.; Syrtanov, M.S.; Lider, A.M. Sintering of MAX-phase materials by spark plasma and other methods. *J. Mater. Sci.* **2021**, *56*, 1980–2015. [[CrossRef](#)]
13. Kashkarov, E.B.; Pushilina, N.S.; Syrtanov, M.S.; Krotkevich, D.G.; Gotman, I.; Travitzky, N. Preceramic paper-derived SiC<sub>f</sub>/Ti<sub>3</sub>Al(Si)C<sub>2</sub> and SiC<sub>f</sub>/Ti<sub>3</sub>SiC<sub>2</sub> MAX-phase based laminates fabricated using spark plasma sintering. *Scr. Mater.* **2021**, *194*, 113696. [[CrossRef](#)]
14. Kashkarov, E.B.; Syrtanov, M.S.; Sedanova, E.P.; Ivashutenko, A.S.; Lider, A.M.; Travitzky, N. Fabrication of paper-derived Ti<sub>3</sub>SiC<sub>2</sub>-based materials by spark plasma sintering. *Adv. Eng. Mater.* **2020**, *22*, 2000136. [[CrossRef](#)]
15. Wang, X.H.; Li, F.Z.; Chen, J.X.; Zhou, Y.C. Insights into high temperature oxidation of Al<sub>2</sub>O<sub>3</sub>-forming Ti<sub>3</sub>AlC<sub>2</sub>. *Corr. Sci.* **2012**, *58*, 95–103. [[CrossRef](#)]
16. Chen, J.; Li, N.; Yan, W. Influence of Ti<sub>3</sub>AlC<sub>2</sub> on corrosion resistance and microstructure of Al<sub>2</sub>O<sub>3</sub>–Ti<sub>3</sub>AlC<sub>2</sub>–C refractories in contact with ladle slag. *J. Eur. Cer. Soc.* **2016**, *36*, 1505–1511. [[CrossRef](#)]
17. Chen, J.; Li, N.; Yan, W.; Wei, Y.; Han, B. Influence of Ti<sub>3</sub>AlC<sub>2</sub> on microstructure and thermal mechanical properties of Al<sub>2</sub>O<sub>3</sub>–Ti<sub>3</sub>AlC<sub>2</sub>–C refractories. *Cer. Int.* **2016**, *42*, 14126–14134. [[CrossRef](#)]
18. Liu, G.; Liao, N.; Nath, M.; Li, Y.; Sang, S. Optimized mechanical properties and oxidation resistance of low carbon Al<sub>2</sub>O<sub>3</sub>–C refractories through Ti<sub>3</sub>AlC<sub>2</sub> addition. *J. Eur. Cer. Soc.* **2021**, *41*, 2948–2957. [[CrossRef](#)]
19. Chen, J.X.; Zhou, Y.C.; Zhang, H.B.; Wan, D.T.; Liu, M.Y. Thermal stability of Ti<sub>3</sub>AlC<sub>2</sub>/Al<sub>2</sub>O<sub>3</sub> composites in high vacuum. *Mater. Chem. Phys.* **2007**, *104*, 109–112. [[CrossRef](#)]

20. Yeh, C.L.; Kuo, C.W.; Chu, Y.C. Formation of  $\text{Ti}_3\text{AlC}_2/\text{Al}_2\text{O}_3$  and  $\text{Ti}_2\text{AlC}/\text{Al}_2\text{O}_3$  composites by combustion synthesis in Ti–Al–C– $\text{TiO}_2$  systems. *J. Alloys Compd.* **2010**, *494*, 132–136. [[CrossRef](#)]
21. Wu, L.; Chen, J.X.; Liu, M.Y.; Bao, Y.W.; Zhou, Y.C. Reciprocating friction and wear behavior of  $\text{Ti}_3\text{AlC}_2$  and  $\text{Ti}_3\text{AlC}_2/\text{Al}_2\text{O}_3$  composites against AISI52100 bearing steel. *Wear* **2009**, *266*, 158–166. [[CrossRef](#)]
22. Hammel, E.C.; Ighodaro, O.R.; Okoli, O.I. Processing and properties of advanced porous ceramics: An application based review. *Cer. Int.* **2014**, *40*, 15351–15370. [[CrossRef](#)]
23. Papynov, E.K.; Portnyagin, A.S.; Modin, E.B.; Mayorov, V.Y.; Shichalin, O.O.; Golikov, A.P.; Avramenko, V.A. A complex approach to assessing porous structure of structured ceramics obtained by SPS technique. *Mater. Character.* **2018**, *145*, 294–302. [[CrossRef](#)]
24. Papynov, E.K.; Shichalin, O.O.; Medkov, M.A.; Grishchenko, D.N.; Tkachenko, I.A.; Fedorets, A.N.; Avramenko, V.A. Spark plasma sintering of special-purpose functional ceramics based on  $\text{UO}_2$ ,  $\text{ZrO}_2$ ,  $\text{Fe}_3\text{O}_4/\alpha\text{-Fe}_2\text{O}_3$ . *Glass Phys. Chem.* **2018**, *44*, 632–640. [[CrossRef](#)]
25. Chen, C.C. Phase Equilibria at Ti–Al Interface Under Low Oxygen Pressure. *Atlas J. Mater. Sci.* **2014**, *1*, 1–11. [[CrossRef](#)]
26. Yang, Z.; Yu, J.; Li, C.; Zhong, Y.; Xuan, W.; Ren, Z.; Wang, H. Preparation of textured porous  $\text{Al}_2\text{O}_3$  ceramics by slip casting in a strong magnetic field and its mechanical properties. *Cryst. Res. Technol.* **2015**, *50*, 645–653. [[CrossRef](#)]
27. Isobe, T.; Kameshima, Y.; Nakajima, A.; Okada, K.; Hotta, Y. Gas permeability and mechanical properties of porous alumina ceramics with unidirectionally aligned pores. *J. Eur. Cer. Soc.* **2007**, *27*, 53–59. [[CrossRef](#)]
28. Dong, Y.; Lin, B.; Zhou, J.E.; Zhang, X.; Ling, Y.; Liu, X.; Hampshire, S. Corrosion resistance characterization of porous alumina membrane supports. *Mater. Character.* **2011**, *62*, 409–418. [[CrossRef](#)]
29. Arratibel Plazaola, A.; Pacheco Tanaka, D.A.; Van Sint Annaland, M.; Gallucci, F. Recent Advances in Pd-Based Membranes for Membrane Reactors. *Molecules* **2017**, *22*, 51. [[CrossRef](#)]
30. Ockwig, N.W.; Nenoff, T.M. Membranes for Hydrogen Separation. *Chem. Rev.* **2007**, *107*, 4078–4110. [[CrossRef](#)]
31. Xomeritakis, G.; Lin, Y.S. Fabrication of a Thin Palladium Membrane Supported in a Porous Ceramic Substrate by Chemical Vapor Deposition. *J. Membr. Sci.* **1996**, *120*, 261–272. [[CrossRef](#)]
32. Lee, D.-W.; Yu, C.-Y.; Lee, K.-H. Synthesis of Pd Particle-Deposited Microporous Silica Membranes via a Vacuum-Impregnation Method and Their Gas Permeation Behavior. *J. Colloid Interface Sci.* **2008**, *325*, 447–452. [[CrossRef](#)]
33. Checchetto, R.; Patel, N.; Miotello, A.; Brusa, R.S. Nanolayers on Nanochannels for Hydrogen Purification. *J. Appl. Phys.* **2009**, *105*, 034502. [[CrossRef](#)]

**Disclaimer/Publisher’s Note:** The statements, opinions and data contained in all publications are solely those of the individual author(s) and contributor(s) and not of MDPI and/or the editor(s). MDPI and/or the editor(s) disclaim responsibility for any injury to people or property resulting from any ideas, methods, instructions or products referred to in the content.